DON'T JUDGE THE MOON BY ITS COVER: GETTING BELOW THE SURFACE WITH MINI-RF. A. M. Stickle[1], G. W. Patterson[1], L. M. Jozwiak[1], A. C. Martin[1], C. A. Nypaver[2], and The Mini-RF Team, [1]Johns Hopkins University Applied Physics Laboratory, 11100 Johns Hopkins Rd., Laurel, MD 20723, angela.stickle@jhuapl.edu; [2]The University of Tennessee, Knoxville, TN

The Aristarchus Region: The Aristarchus Plateau on the lunar nearside is characterized by a variety of interesting geological features. The plateau itself is surrounded by flood basalts of Oceanus Procellarum, is oddly shaped, and has extreme high and low reflectance areas (e.g., Figure 1A). The rille, Vallis Schröter, cuts through the plateau, which is also nearly covered by a large pyroclastic deposit thought to be between 20-30m thick [1] and dominated by low-Ti glass spheroids [e.g., 2-3] (Figure 1D). A set of streaks, which are generally radial to Aristarchus crater, have been observed in multiple wavelengths (e.g., optical, radar) across the plateau. Aristarchus, Prinz, and Herodotus craters are all clearly visible in Lunar Reconnaissance Orbiter Camera (LROC) imagery and topographic data (Figure 1A, 1B). The incomplete crater rim of Herodotus E is clearly seen in topography and geologic maps (Figure 1B, 1D). This eroded rim, however, is not as apparent in thermal data, or visible imagery at high incidence angles (Figure 1A, 1C). Because radar is sensitive to roughness, and can also probe beneath the surface, Mini-RF data can provide a different view of, and potentially other insights into, the geology of the region.

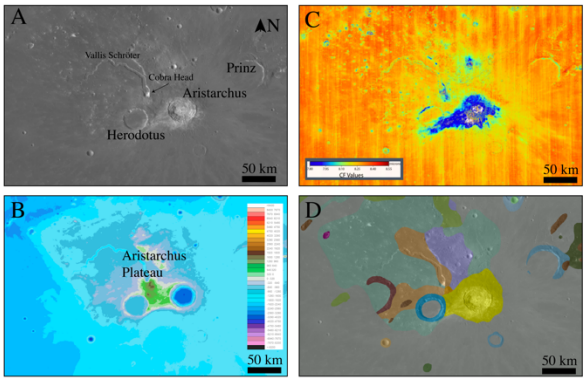

Figure 1. A) LROC WAC image of the Aristarchus Plateau; B) Topography of the Aristarchus Plateau from the SLDEM2015 DEM [4]; C) Diviner Christiansen Feature (CF) map of the Aristarchus Plateau [5]. Lower CF values correspond to more silicic material; D) Geologic map of the Aristarchus Plateau, showing an updated version of the I-0703 Wilhelms Geologic map of the nearside at 1:5,000,000 [6].

The Mini-RF Radar: The Mini-RF instrument aboard NASA's Lunar Reconnaissance Orbiter (LRO) is a hybrid-polarized, dual-frequency synthetic aperture radar (SAR) [7,8] that operates in cooperation with the DSS-13 Goldstone Deep Space Communications Complex and the Arecibo Observatory (AO) [9,10] to collect S- and X-band (12.6 cm and 4.2 cm wavelength, respectively) bistatic radar measurements of the lunar nearside and poles. For each observation, the surface is illuminated with a circularly polarized, chirped signal that tracks the Mini-RF antenna boresight intercept on the surface of the Moon. The Mini-RF receiver operates continuously, separately receiving the horizontal and vertical polarization components of the signal backscattered from the lunar surface. In this architecture, the incidence angle varies as a function of the observation geometry and the data have a spatial resolution of ~100 m in range and ~2.5 m in azimuth. This can vary from one observation to another as a function of the viewing geometry. The data are coherently processed onto grids with a spacing of 4 m along track and 25 m cross track. For analysis, they are then incoherently reduced to a uniform 100 m grid yielding approximately a 25-look average for each sampled location.

The data returned provide information on the structure (i.e., roughness) and dielectric properties of surface and buried materials within the penetration depth of the system (up to several meters for Mini-RF) [11-14]. Laboratory data and analog experiments at optical wavelengths have shown that the scattering properties of lunar materials can be sensitive to variations in bistatic angle [15-17]. The bistatic architecture also allows examination of the scattering properties of a target surface for a variety of bistatic angles to evaluate differences in scattering properties at radar wavelengths.

To date, 33 S-band and 44 X-band bistatic observations have been collected of the lunar nearside and poles. Recent improvements to the time-domain back-projection algorithm that processes the radar data into images [18] have led to significant improvements in image focusing and in topographic control. The improved topographic control has been facilitated by the inclusion of low-resolution (LOLA LDEM4) topography in the image formation process. A result of including these data is the modification of the existing image cube and the inclusion of additional backplanes to each cube (i.e., elevation and slope) (e.g., Figure 2). As an example of the newly re-processed data, we examine the Aristarchus region, which was originally collected by the Mini-RF radar on October 30, 2012. Improved data quality resulting from new processing techniques

reveals additional features in the Aristarchus region that are less apparent in other data sets (e.g., Fig. 3).

Seeing Beneath the Surface: Radar data can be used to identify features not easily seen in visible images. For example, the crater Herodotus E is clearly visible in Mini-RF CPR (roughness) data (Figure 3D), though it is not easily discernible in high phase LROC optical imagery (Figure 3A). Other intriguing features are present on the Aristarchus plateau, including streaks that are clearly visible in optical images, show up as bright in the radar image (Figure 3B). The streaks across Aristarchus are also seen in Earth-based radar data [19]. These streaks, though still present, are less clearly defined in the CPR image (Figure 3C).

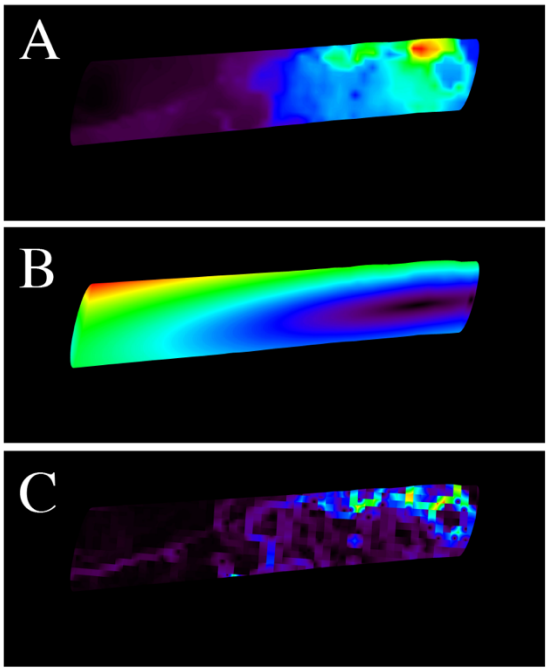

Figure 2. Examples of new backplanes available with the Mini-RF bistatic data. A) Height of the surface used in processing of the data; B) Bistatic angle across the collect; c) Slope of the surface used in data processing.

Acknowledgments: This work was funded by the Mini-RF Project.

References: [1] McEwen et al. (1994) *Science, 266,* 1858–1862; [2] Lucey et al. (1986) *Proc. Lunar and Planet. Sci. Conf. 16th, J. Geophys. Res., 91, Suppl.,* D344–D354; [3] Mustard et al. (2011), *J. Geophys. Res. Planets*; [6] Fortezzo, C.M. and T.M. Hare (2013), *LPSC XLIV,* Abstract #2114; [4] Barker et al. (2015) *Icarus,* 273, pp. 346-355; [5] Greenhagen et al. (2010), *Science*, 329(5998); [7] Chin et al., 2007, Space Sci. Rev. 129(4), 391-419; [8] Nozette et al., 2010, Space Sci. Rev., 150, 285-302; [9] Patterson et al., 2013, 44th LPSC, #2380; [10] Patterson et al., 2017, Icarus, 283, 2-19; [11] Campbell et al. (2010), *Icarus*, 208, 565-573; [12] Raney et al. (2012), *JGR,* 117, E00H21; [13] Carter et al. (2012), *JGR,* 117, E00H09; [14] Campbell (2012), *JGR*, 117, E06008; [15] Hapke et al. (1998), *Icarus*, 133, 89-97; [16] Nelson et al. (2000), *Icarus*, 147, 545-558; [17] Piatek et al. (2004), *Icarus*, 171, 531-545; [18] F.S. Turner et al. (2019) 4th Data Users Workshop, Abstract #7075; [19] Campbell B.A. et al, (2008) *Geology*, 208, 135.

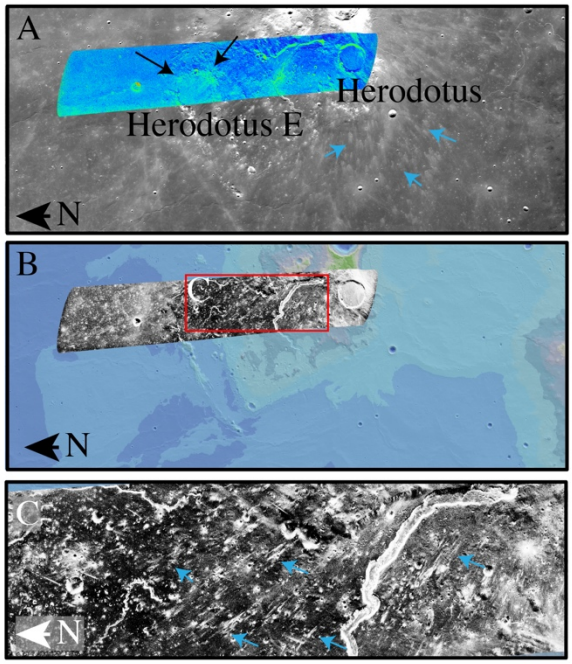

Figure 3. A) Radar CPR (roughness) (λ=12.6 cm) image of the Aristarchus Plateau and Herodotus crater, overlain on the LROC WAC image. Black arrows show the rim of the ancient crater Herodotus E (48 km dia.), while blue arrows indicate streaks radial to Aristarchus crater. B) Total power returned to the Mini-RF radar from backscattered energy overlain on the LDEM256 radar shaded topography. C) Close-up of (B) for area indicated by a red box, showing Mini-RF data for a portion of the Aristarchus Plateau. Blue arrows indicate radar bright streaks approximately radial to Aristarchus crater